Electronic Supplementary Information

Chemical synthesis of binder-free nanosheets like cobalt vanadium oxide thin film electrodes for hybrid supercapacitor devices

Sambhaji S. Kumbhar[a], Shraddha B. Bhosale[a], Sumita S. Patil[a], Akshay Ransing[b], Vinayak G. Parale[b], Chandrakant D. Lokhande[a], Hyung-Ho Park[b*] and Umakant M. Patil[a,b*]

[a]Centre for Interdisciplinary Research, D. Y. Patil Education Society, Kasaba Bawada, Kolhapur-416006 (India)

[b]Department of Materials Science and Engineering, Yonsei University, 50 Yonsei-ro, Seodaemun-gu, Seoul-03722, (Korea)

Content	Page No.

Note S1: Formulae for calculations

Crystallinity calculation:

$$\text{Crystallinity (\%)} = \frac{\text{Area of crystalline peaks}}{\text{Area of all peaks}} \times 100 \qquad \text{(F1)}$$

For the three-electrode system:

The specific capacitance of C-CV electrodes is calculated from GCD analysis using following equation,

$$Cs = \frac{I \times \Delta t}{m \times \Delta V} \qquad (\text{F g}^{-1}) \qquad \text{(F2)}$$

Where I, Δt, m, and ΔV are current density, discharging time, mass of active material, and potential window, respectively. Furthermore, the specific capacity of the C-CV series electrodes from the GCD analysis is measured using below equation [R1],

$$Q = \frac{I \times \Delta t}{m} \qquad (\text{C g}^{-1}) \qquad \text{(F3)}$$

For two electrode systems:

The charges between the cathode and anode balanced for excellent electrochemical results of AHSD and SH-FSD devices by using the theory of mass balance as per the following equation [R2],

$$\frac{m_+}{m_-} = \frac{C_- \times \Delta V_-}{C_+ \times \Delta V_+} \qquad \text{(F4)}$$

where m_+, C_+, and ΔV_+ are the mass of positive material, positive material capacitance, and potential window of positive material, respectively. Also, m_-, C_-, and ΔV_- are the mass of negative material, negative material capacitance, and potential window of negative material, respectively.

The two-electrode system was used to study hybrid device performance, and its specific energy (SE) and specific power (SP) were calculated using the following equations respectively [R3],

$$SE = \frac{C_s \times (\Delta V)^2}{2 \times 3.6} \qquad (\text{Wh kg}^{-1}) \qquad \text{(F5)}$$

$$SP = \frac{E \times 3.6}{\Delta t} \qquad (\text{kW kg}^{-1}) \qquad \text{(F6)}$$

where, C_s, ΔV, and Δt represent specific capacitance, potential window, and discharging time of the device, respectively.

Note S2: Preparation of rGO

Graphene oxide (GO) was synthesized using a modified version of Hummer's method, and the reduction of GO's functional groups was accomplished with the assistance of hydrazine hydrate [R4]. Following is a detailed explanation of the complex procedure used to create reduced graphene oxide (rGO): Initially, 1 mg mL^{-1} of GO powder was fully dispersed using ultrasonication. The dispersed solution was added to a flask with a spherical bottom, set up using a method similar to reflux, and then heated to 368 K. Subsequently, hydrazine hydrate was introduced, and the reaction was maintained at a consistent temperature for a duration of 3 hrs. Following the completion of the reaction, the solution underwent centrifugation for 2-3 cycles and was subjected to thorough washing with DDW. Ultimately, the resulting product was freeze-dried and subsequently utilized for the construction of a negative electrode.

Note S3: PVA-KOH gel preparation

The fabrication of a solid-state hybrid supercapacitor device involved the blending of polyvinyl alcohol (PVA) with potassium hydroxide (KOH) to form an electrolyte gel. The dissociation of 1.5 g of PVA occurred in 15 ml of DDW at a temperature of 343 K under vigorous stirring. Subsequently, the PVA solution was mixed with 5 ml of a 1 M KOH solution while maintaining continuous agitation, resulting in the formation of a dense and transparent solution. This gel was employed as a separator and electrolyte for the fabrication of the solid device.

Note S4: Reaction mechanism

Hydrous thin films of cobalt vanadium oxide were fabricated on SS substrates utilizing a straightforward CBD method. This method recognized as an effective 'bottom-up' strategy for nanostructure synthesis, relies on the creation of a solid phase from solutions via a heterogeneous reaction. This process encompasses three successive stages: nucleation, coalescence, and particle growth. Hydrous cobalt vanadium oxide thin films of C-CV series (C-CV1, C-CV2, C-CV3, C-CV4, and C-CV5) are prepared to scrutinize the effect of concentration ratio variation and five different reaction baths consisting of different precursor concentrations (Co:V) along with 0.05 M urea (hydrolyzing agent) dissolved in aqueous bath heated at 368 K constant temperature for 9 h, as schematically shown in Figure 1. In the formation of C-CV thin films, different reaction steps take place, as given below,

Initially, dissociation of cobalt chloride hexahydrate in the DDW takes place, as per reaction (F7), and dissociates into Co^{2+} and Cl^- ions.

$$CoCl_2 \cdot 6H_2O + H_2O \rightarrow Co^{2+} + 2Cl^- \tag{F7}$$

Similarly, ammonium metavanadate simultaneously dissociates in DDW as per the following equation (F8)

$$NH_4VO_3 \leftrightarrow NH_4^+ + VO_3^- \tag{F8}$$

Moreover, urea is crucial in controlling hydrolysis through delayed breakdown. This includes the decomposition of urea at 368 K as per equation (F9), which produces ammonia (NH_3) and carbon dioxide (CO_2).

$$CO(NH_2)_2 \rightarrow NH_3 + HNCO \tag{F9}$$

Urea decomposition makes the solution alkaline, and alkaline conditions are most relevant to the formation of complexes with metal ions and metavanadate [R5]. Finally, to cause an overall reaction (F10) causes for C-CV samples formation as follows,

$$Co(NH_3)^{2+} + Cl^- + 2VO_3^- + nH_2O \rightarrow CoV_2O_6 \cdot nH_2O + NH_4Cl \qquad \text{(F10)}$$
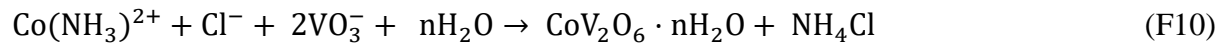
According to the above reaction mechanism, the growth of consistently brown-colored C-CV thin films was effectively achieved by optimizing the deposition period at low temperatures. Notably, it was found that the C-CV thin films were not optimally uniform before 9 h reaction duration and that after this duration, a powdery film developed because of excessive material growth, which caused the film's outer layer to peel off.
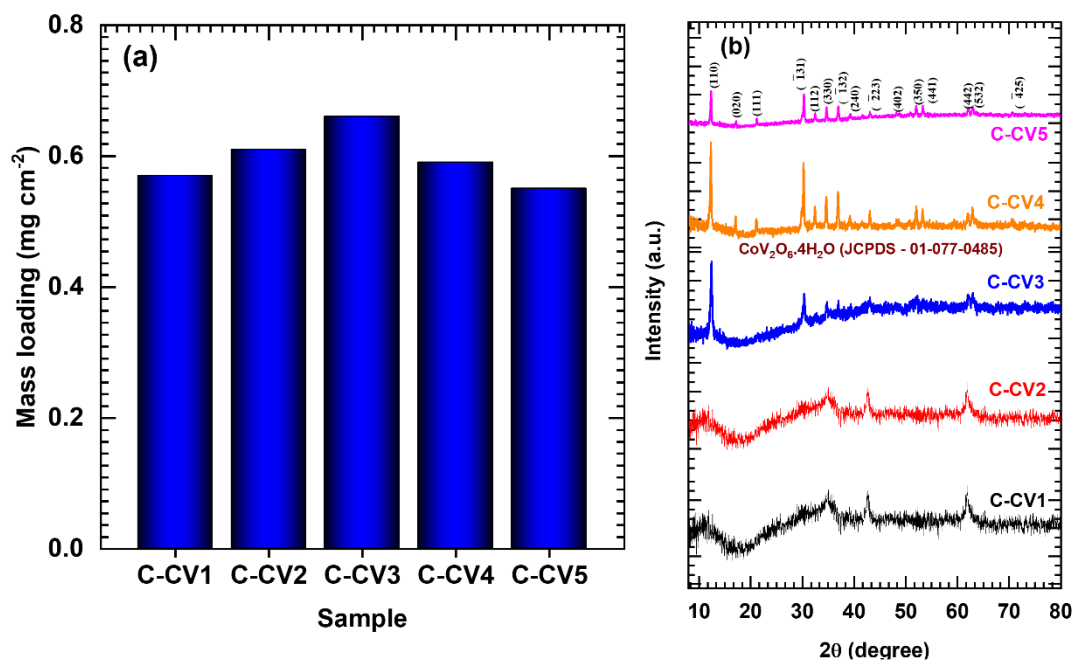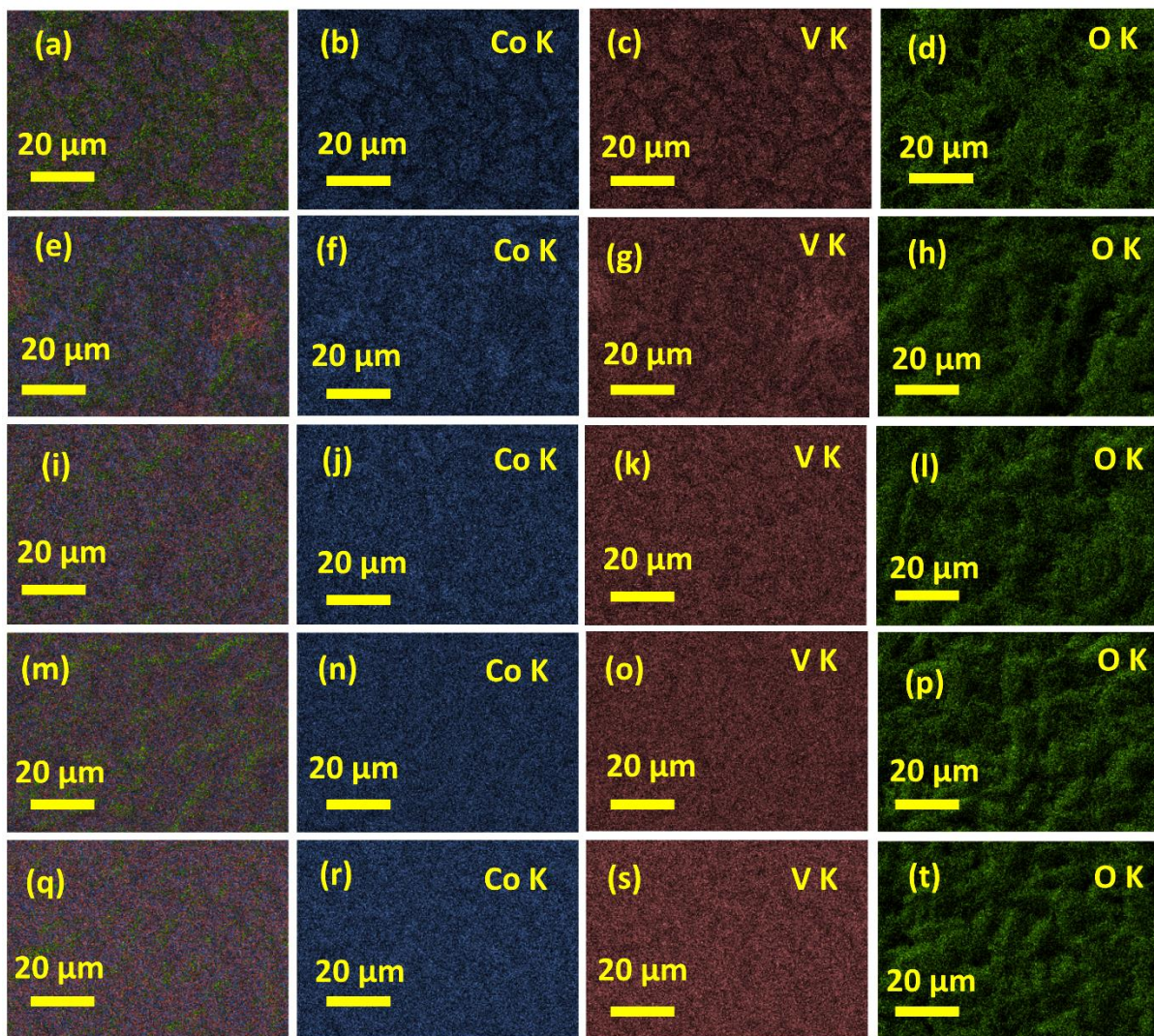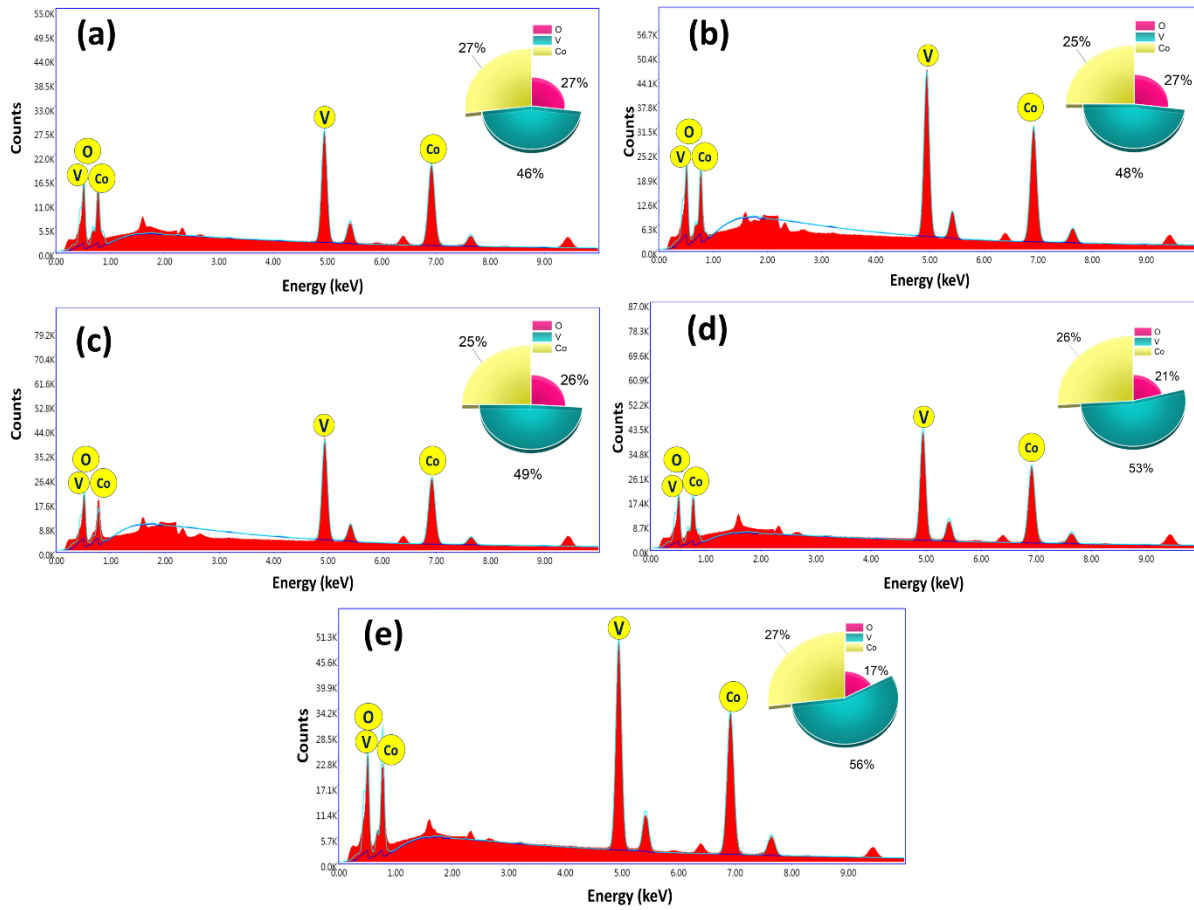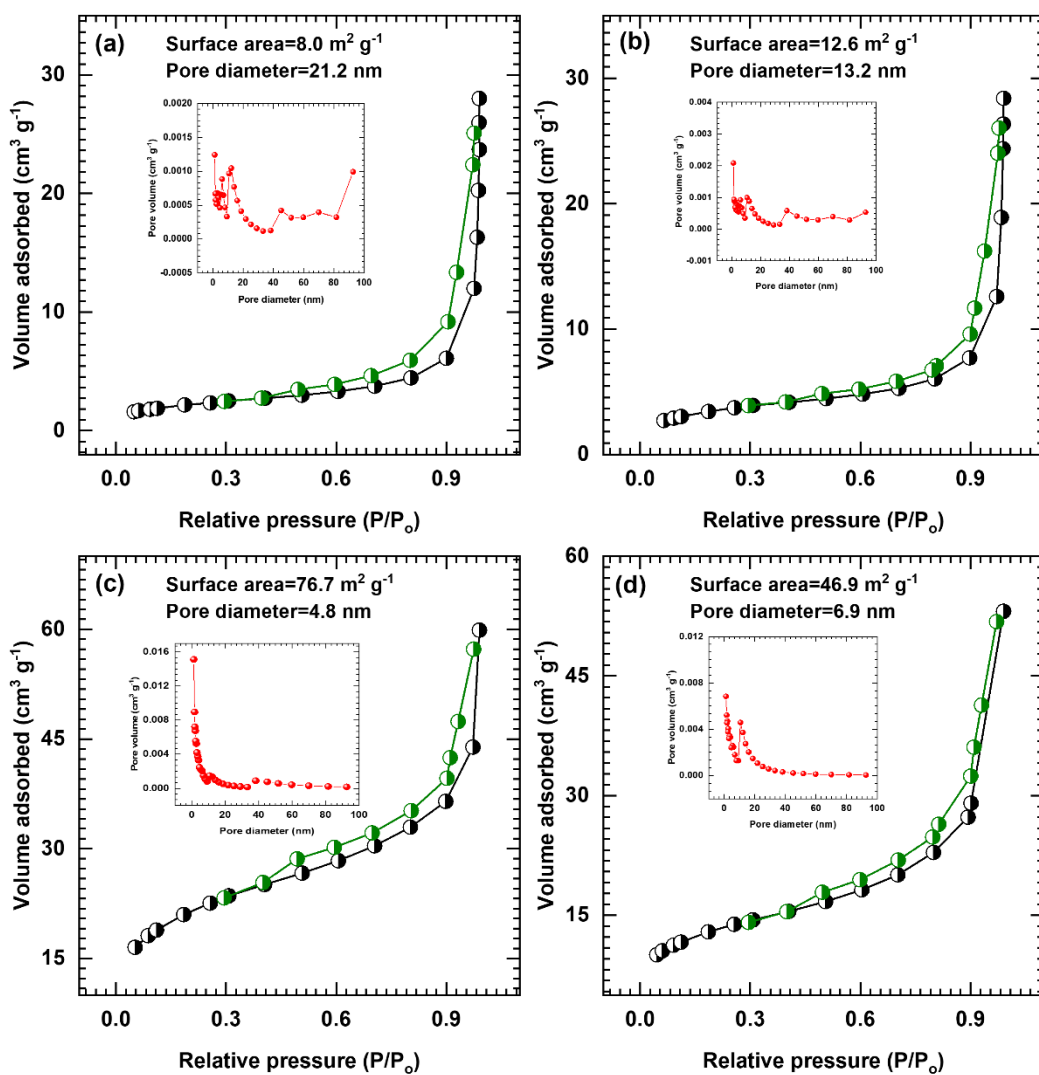
Fig. S1

Fig. S2

Fig. S3

Fig. S4

Note S5: Electrochemical performance of C-CV0 electrode.

The cobalt carbonate hydrogen hydrate thin film electrode (C-CV0) was tested in 1 M KOH electrolyte using a three-electrode system. Fig. S5(a) shows the CV curves at different scan rates, such as 2-100 mV s^{-1}, where a couple of redox peaks are observed. The scan rate-dependent CV curves indicate that the area under the CV curves increases with increasing scan rates, indicating that the voltammetry current is proportional to the scan rate. A study of charge kinetics was conducted to analyze the mechanisms involved in charge storage for the thin film electrode of the C-CV0 sample. The current contribution of surface-controlled and diffusion-controlled for the C-CV0 electrode is calculated at various scan rates and presented in Fig. S5(b), where more surface contribution (Qs) is observed. The GCD analysis was executed within the optimized potential window of 0 to 0.5 V, as shown in Fig. S5(c). The GCD curves of the C-CV0 electrode at various current densities from 1 to 5 A g^{-1} were carried out. At a current density of 1 A g^{-1}, the maximum specific capacitance of 97.3 F g^{-1} is obtained. Additionally, the electrode of the C-CV0 sample was the subject of an EIS study; the EIS plot with an inset fitted circuit is displayed in Fig. S5(d). For the C-CV0 electrode, the fitted values of R_s and R_{ct} are 0.83 and 745 Ω, respectively.
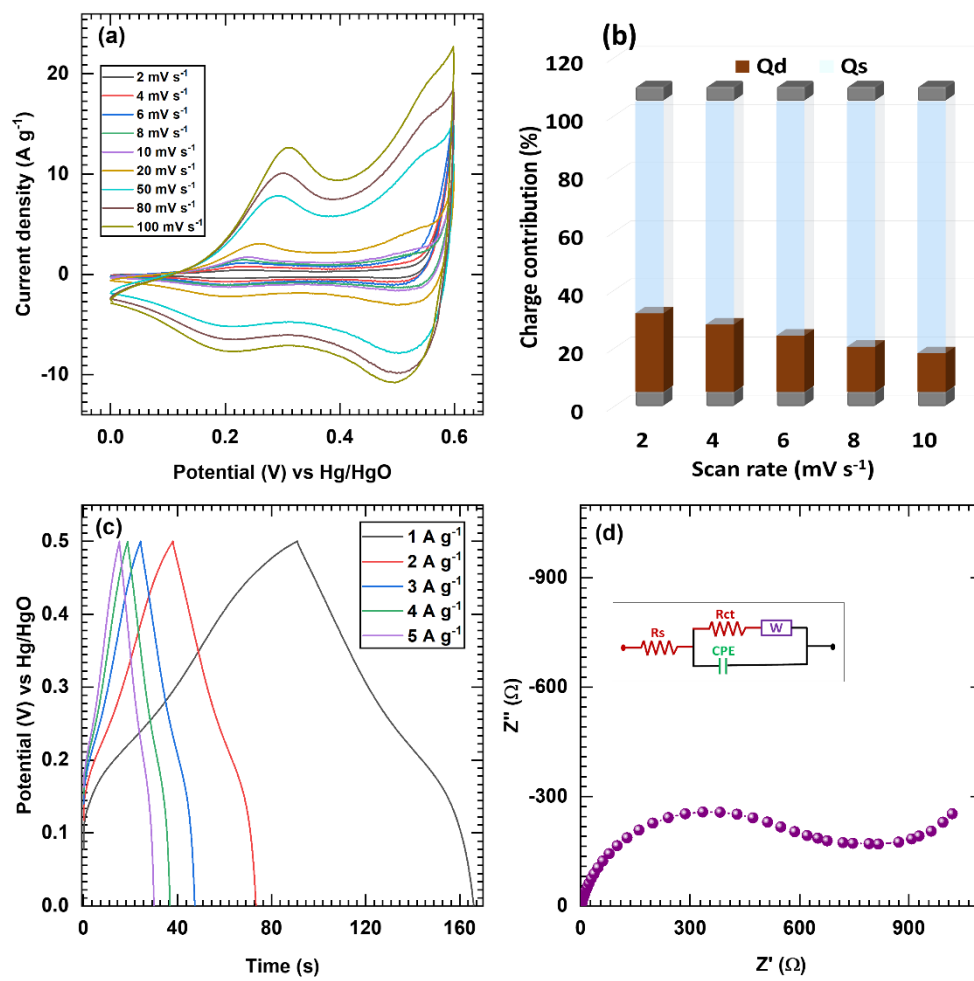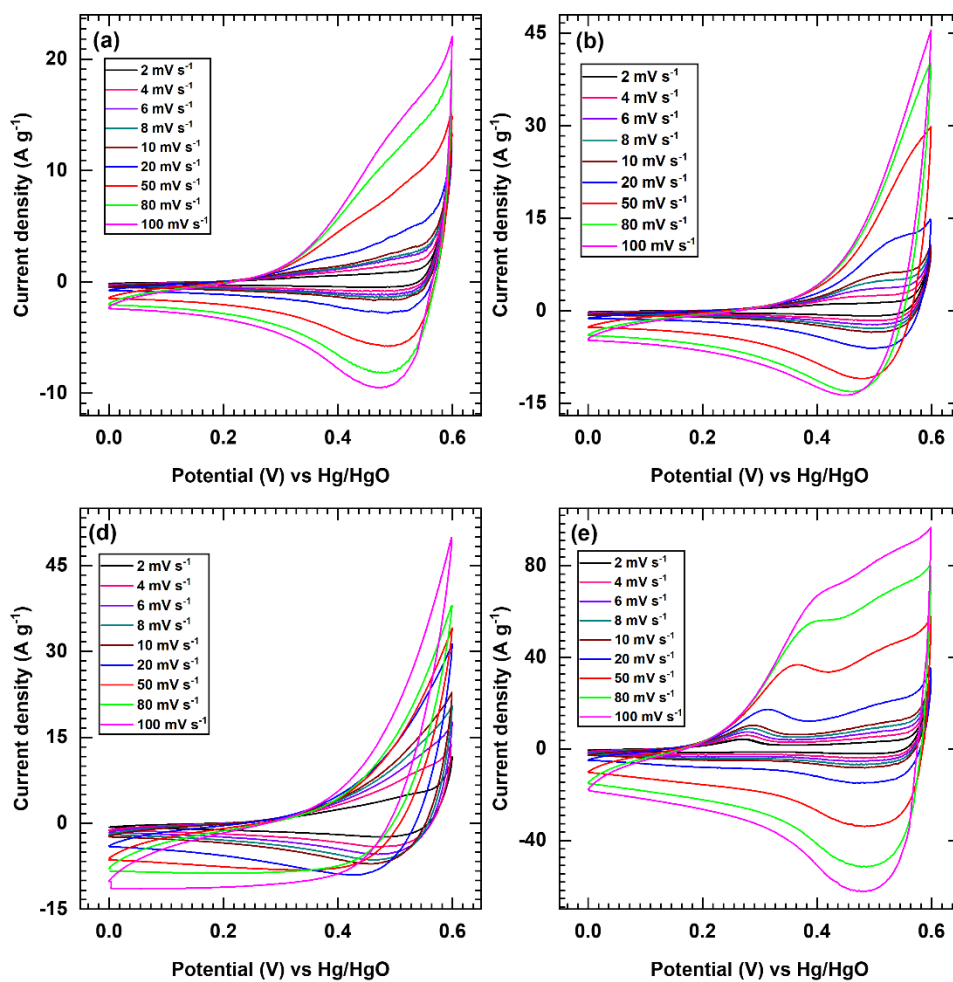
Fig. S5

Fig. S6

Note S6: Charge contribution of C-CV series electrodes

The charges stored by surface capacitive and bulk intercalation processes in C-CV electrodes. Hence, the power law equation given below (equation F11) is used to calculate the contributions of surface capacitive control and diffusion control to determine the charge storage mechanism of the C-CV series electrodes [R6]:

$$i = a v^b \tag{F11}$$

In equation (F11), where both 'a' and 'b' are variables that can be changed, the value of parameter 'b' is calculated by comparing the slopes of log (i) and log (v) plots. The parameter 'b' is most relevant on different values of 0.5 and 1, where the first value (0.5) denotes diffusion-limited faradaic intercalation and the second value (1) represents the capacitive behaviour of the material.

The total charge stored capacity (Q_{total}) of C-CV electrodes can be separated into two parts: surface capacitive (Q_s) and diffusion controlled (Q_d), as given in the equation below.

$$Q_{total} = Q_s + Q_d \tag{F12}$$

Where Q_{total} refers to the total stored charge, Q_s denotes the charge stored at the surface of the material and is related to the electric double-layer capacitors (EDLCs). On the other hand, Q_d represents the redox reactions that occur in the bulk of the material, resulting from a sluggish diffusion process [R7]. The charge storage kinetic analysis uses CV curves measured at various scan rates to distinguish between the multiple contributions. Particularly, Q_s can be calculated using the equation below under the assumption of semi-infinite linear capacitive behaviour with scan rates.
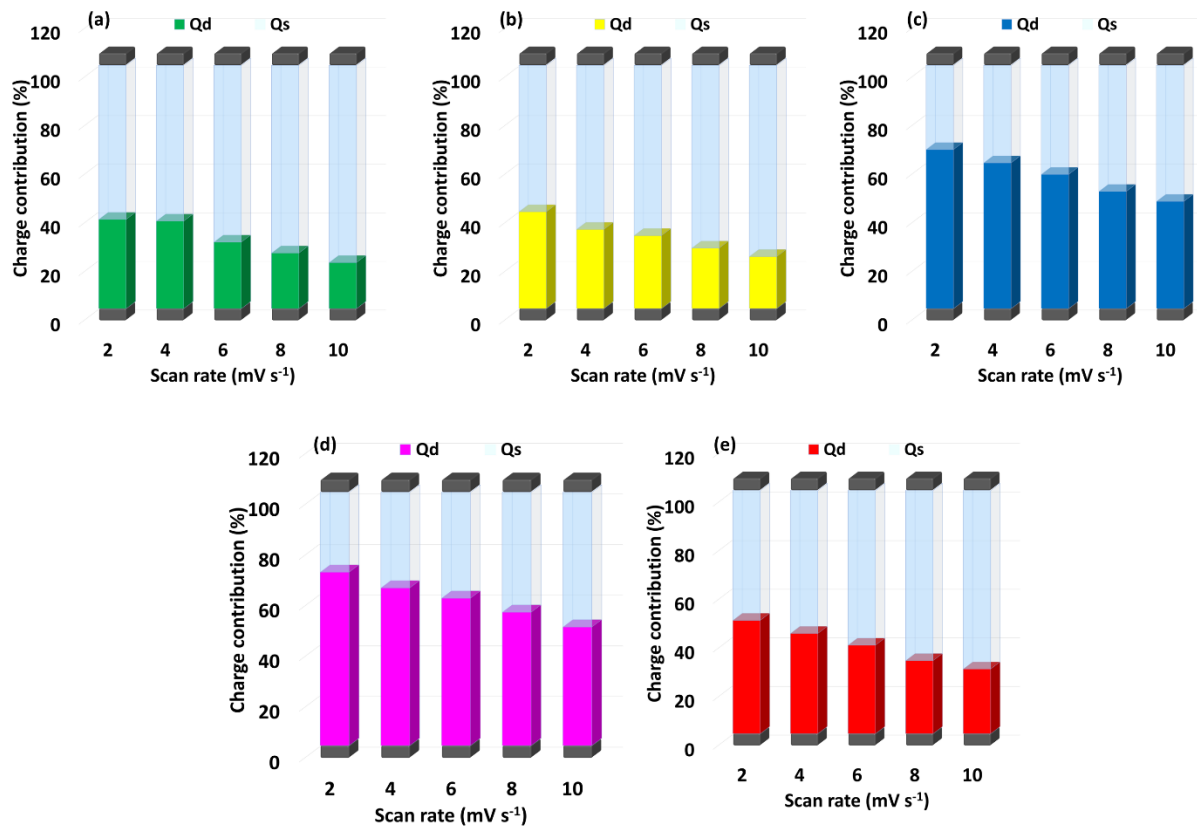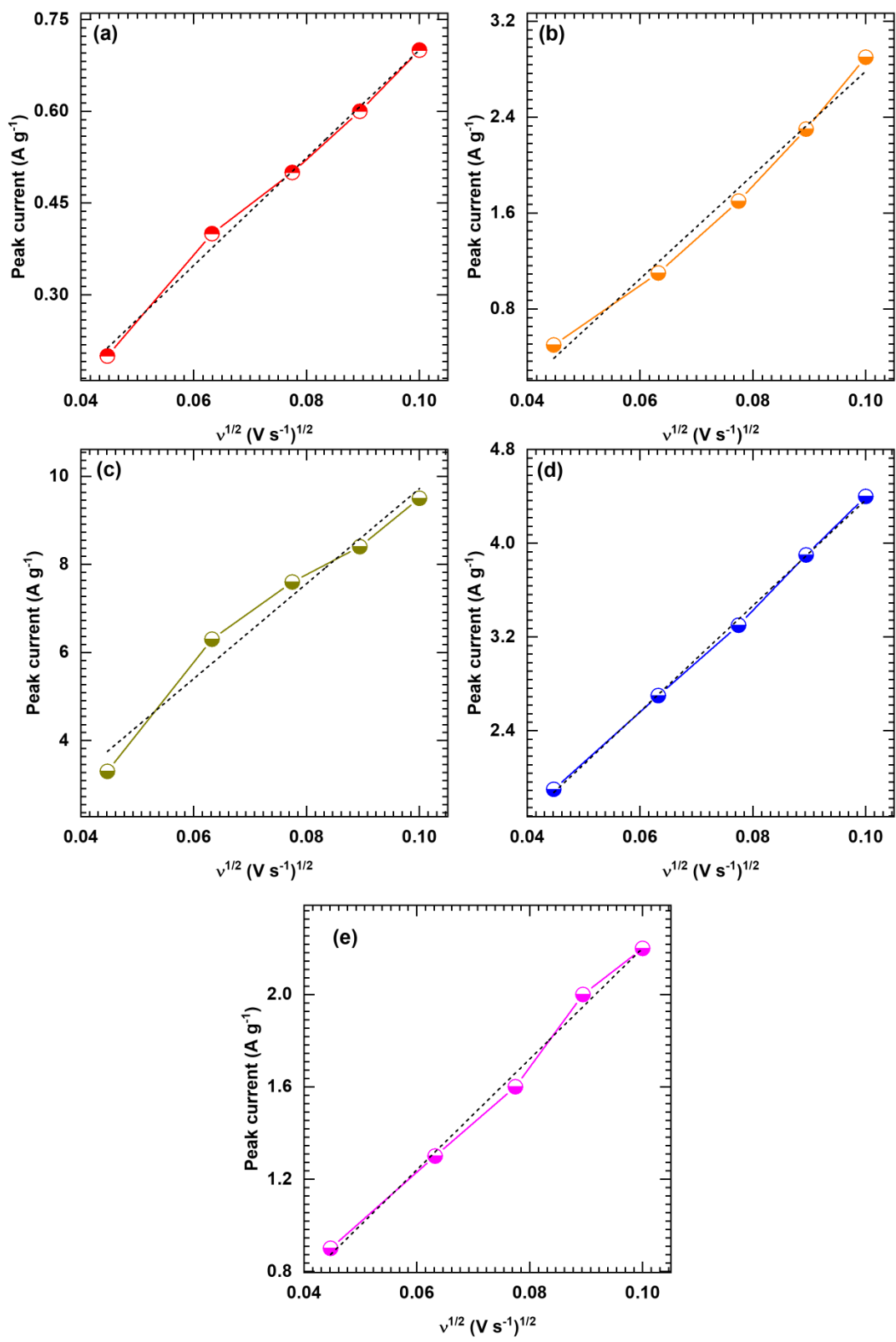
$$Q_{total} = Q_s + Const. v^{-1/2} \tag{F13}$$
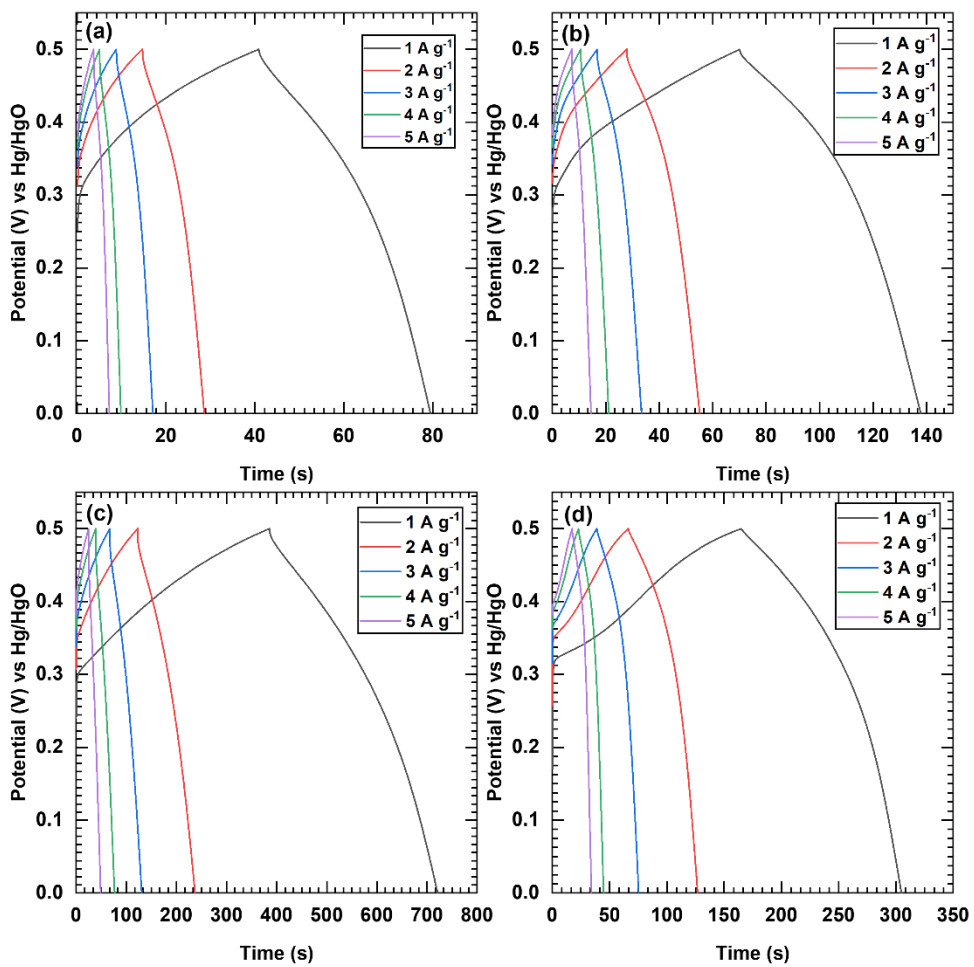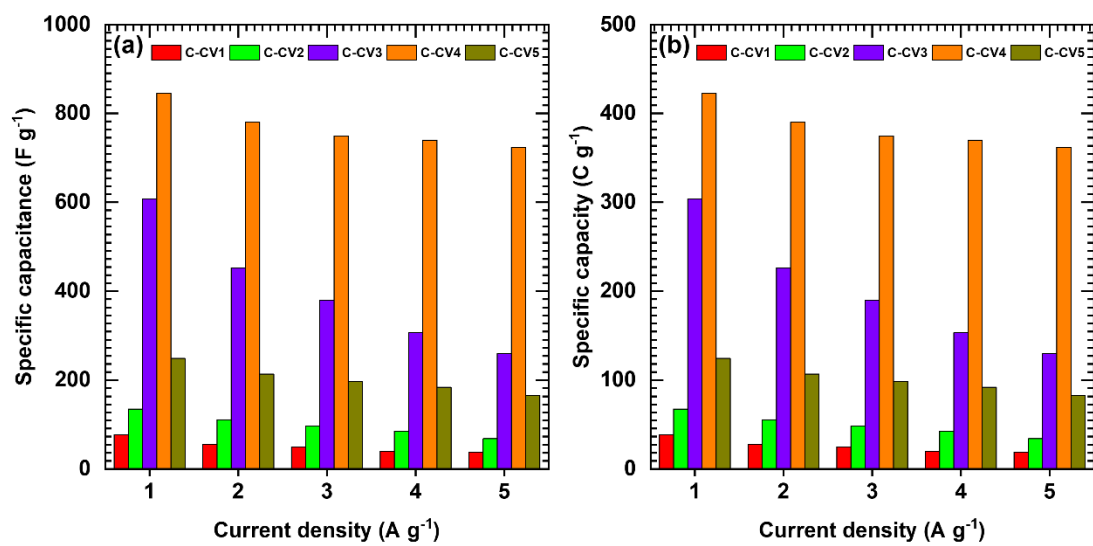
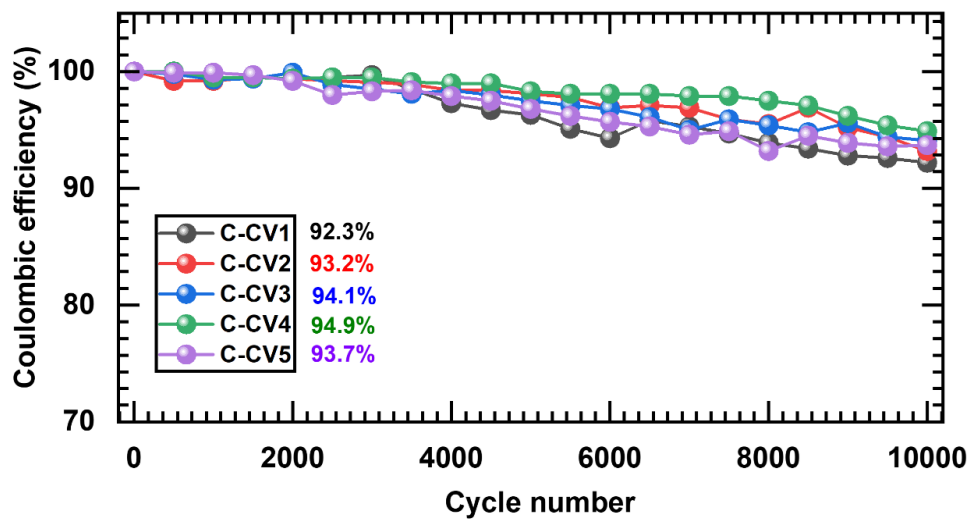**Fig. S7**

Fig. S8

Fig. S9

Fig. S10

Fig. S11

Note S7: After cycling XRD and FE-SEM analysis

To assess the stability of the phase and morphological structure of the C-CV electrode, structural and morphological analysis of the optimized C-CV4 electrode was conducted using XRD and FE-SEM techniques after prolonged electrochemical cycling (10,000 GCD cycles). Post-electrochemical cycling, the C-CV4 electrode exhibits pronounced diffraction peaks of (110), (111), (330), and ($\bar{1}$32), with a reduction in intensities than before the stability test, as depicted in Fig. S12(a). Additionally, the morphology of the C-CV4 electrode shows slight alterations post-cycling, as illustrated in FE-SEM images at different magnifications of 1KX, 10KX, and 40KX in Fig. S12(b-d). At low magnification (Fig. S12), it is clearly seen that the nanosheet-like morphology of the C-CV4 electrode is well maintained and looks similar to before electrochemical measurements. However, the average thickness of the nanosheets (~72 nm) is slightly reduced after the electrochemical stability as the FE-SEM image shown at higher magnification (Fig. S12(c)) and histogram in Fig. S12(e). Moreover, the rough surface of nanosheets is observed at higher magnification (Fig. S12(d)) due to dendrites formation owing to the development of a hydroxide phase. Thus, the negligible change in structural phase and surface morphology with a reduction in nanosheet thickness indicates less damage in the nanosheets-like microstructure of C-CV4 material, which confirms good electrochemical stability.
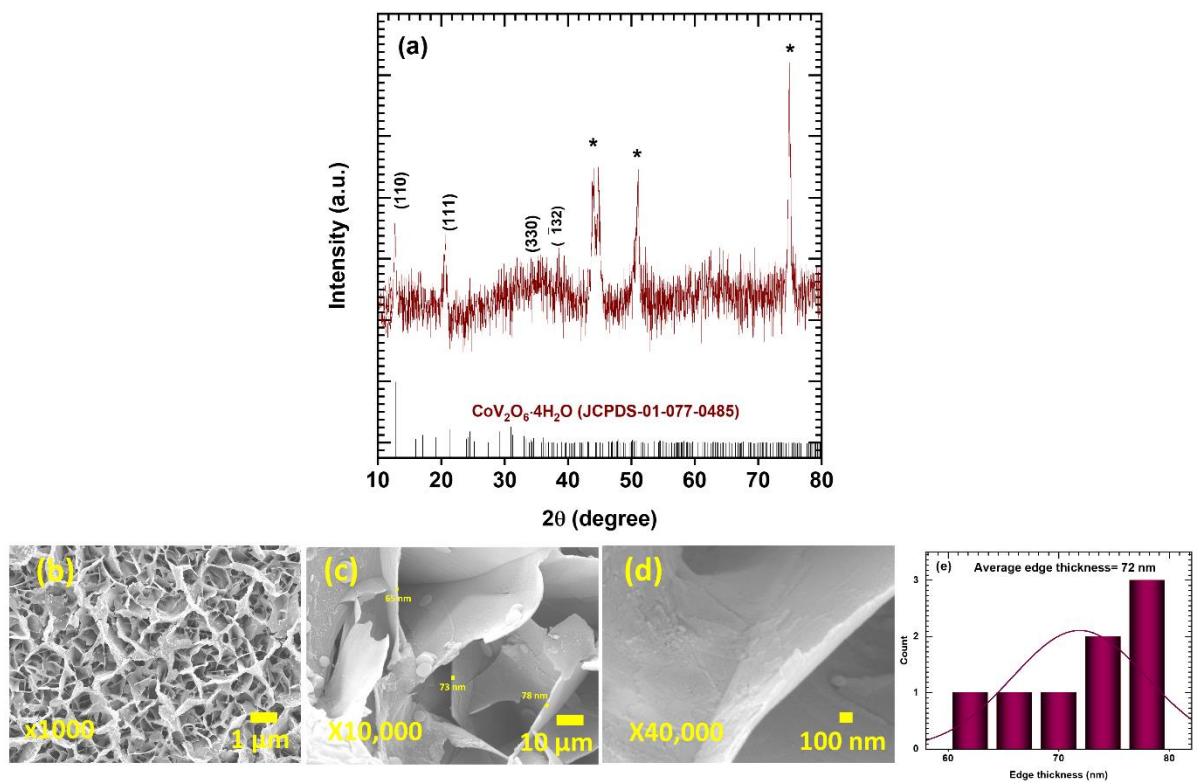
Fig. S12

Note S8: Characterizations of rGO electrode material.

Fig. S13 (a) displays the GO and rGO XRD patterns. Successful production of GO and the generation of rGO are confirmed by the intense characteristic peaks at 24.1° and 43° in the XRD, respectively. Successful conversion of GO to rGO is demonstrated by a shift in peak from 10.5° to 24.1°. The XRD data show that the hydrazine hydrate reduces GO to rGO successfully.

Fig. S13 (b) displays the CV curves of the rGO electrode at different scan rates between 5 and 100 mV s^{-1} in the optimal potential window between -1 and 0 V/Hg/HgO in 1 M KOH electrolyte. The quasi-rectangular shape of the CV curves supports the rGO electrode's EDLC-based capacitive nature. Fig. S13 (c) displays the GCD analysis of the rGO electrode. For the rGO electrode, the almost linear charge-discharge curves are obtained, demonstrating its double-layer capacitive nature. For the rGO electrode, a specific capacitance of 290 F g^{-1} is obtained at a current density of 2 A g^{-1}. Fig. S13 (d) displays the Nyquist plot of the rGO electrode. The fitted circuit is displayed in Fig. S13 (d) inset. Rs is the solution resistance in the fitted circuit (0.95 Ω), R$_{ct}$ is the charge transfer resistance (4.35 Ω), W is the Warburg impedance (8.11 Ω), and CPE is the general imperfect capacitor (0.19 mF) with a 0.88 correction factor (n).
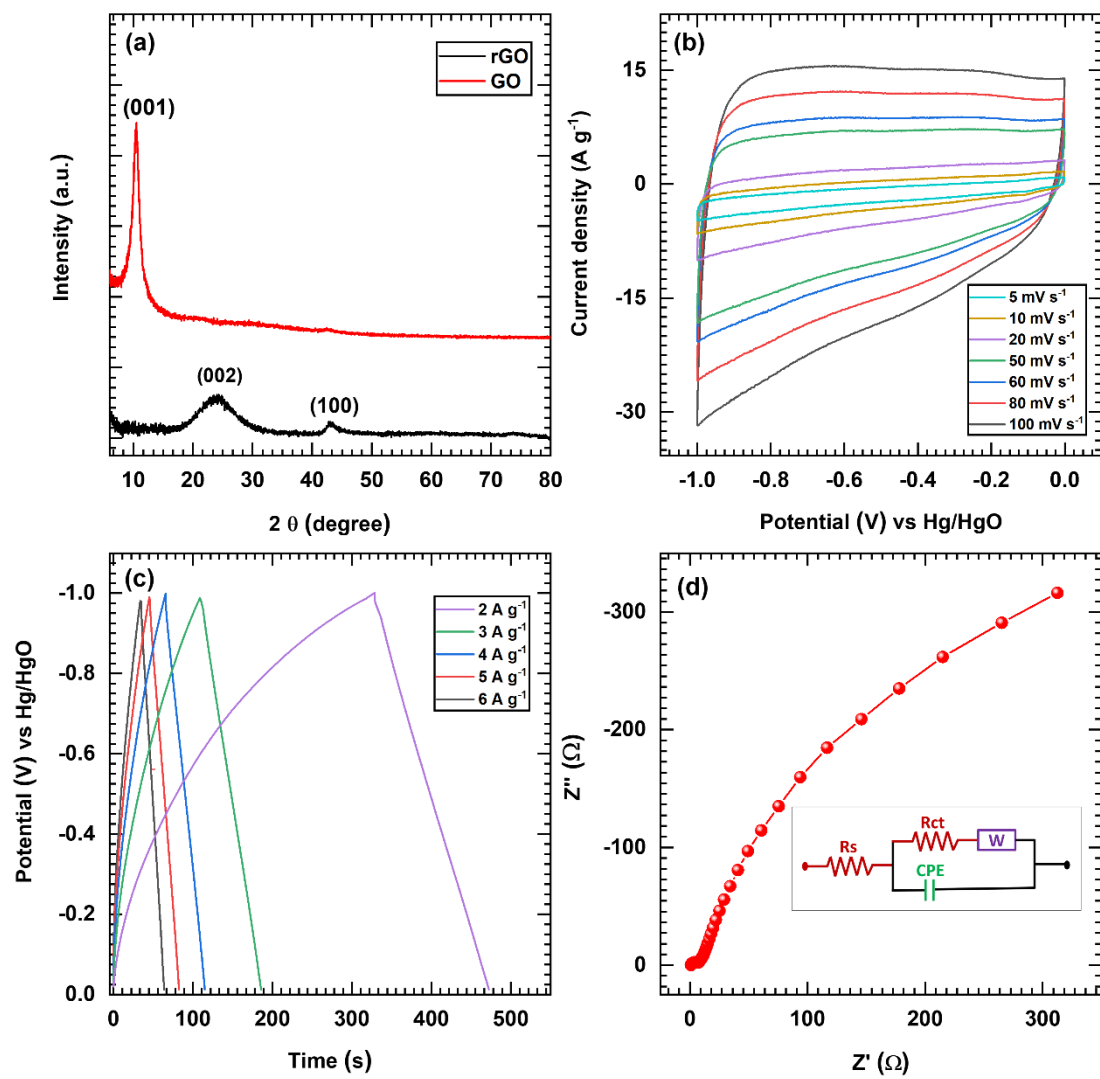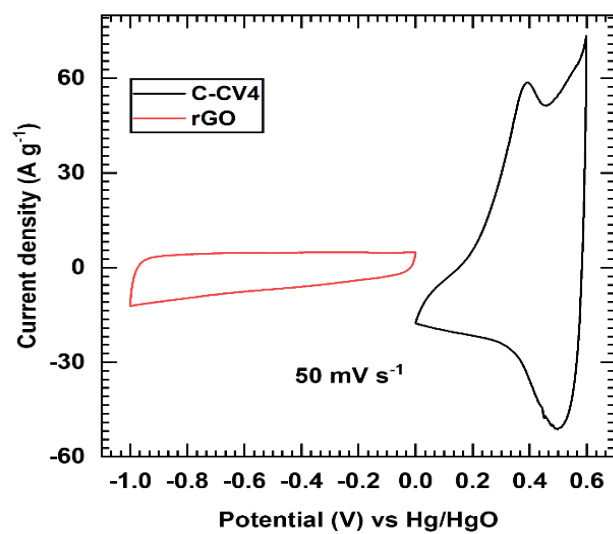
Fig. S13

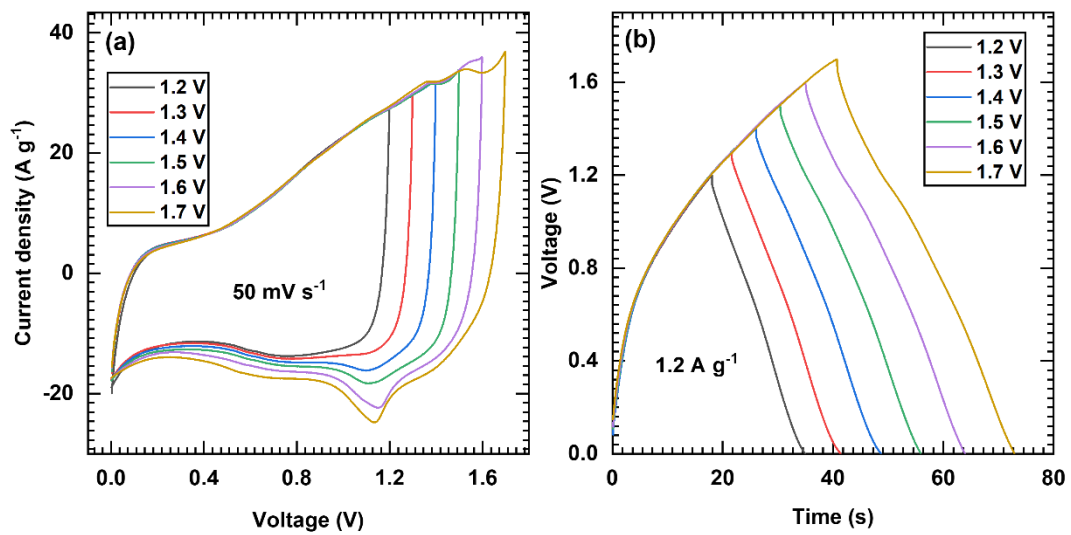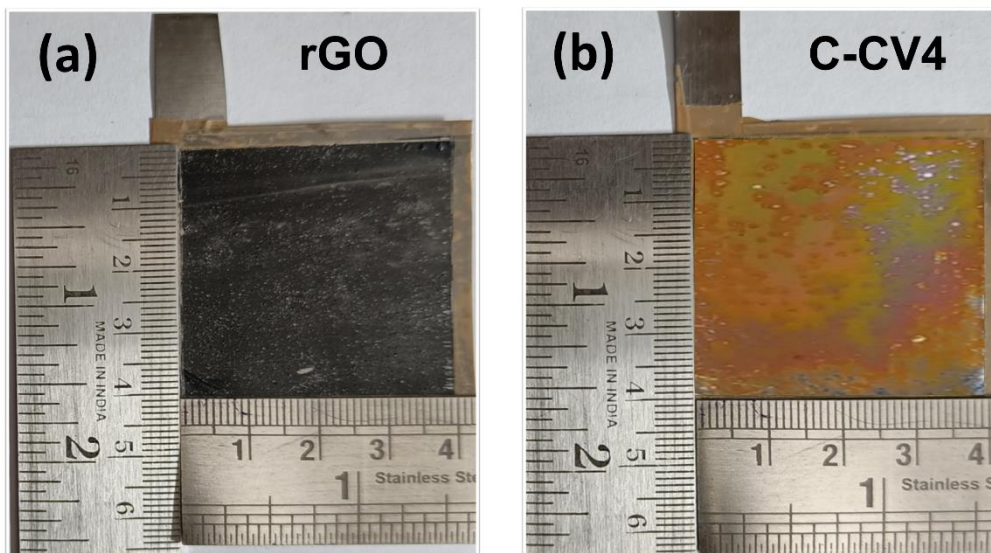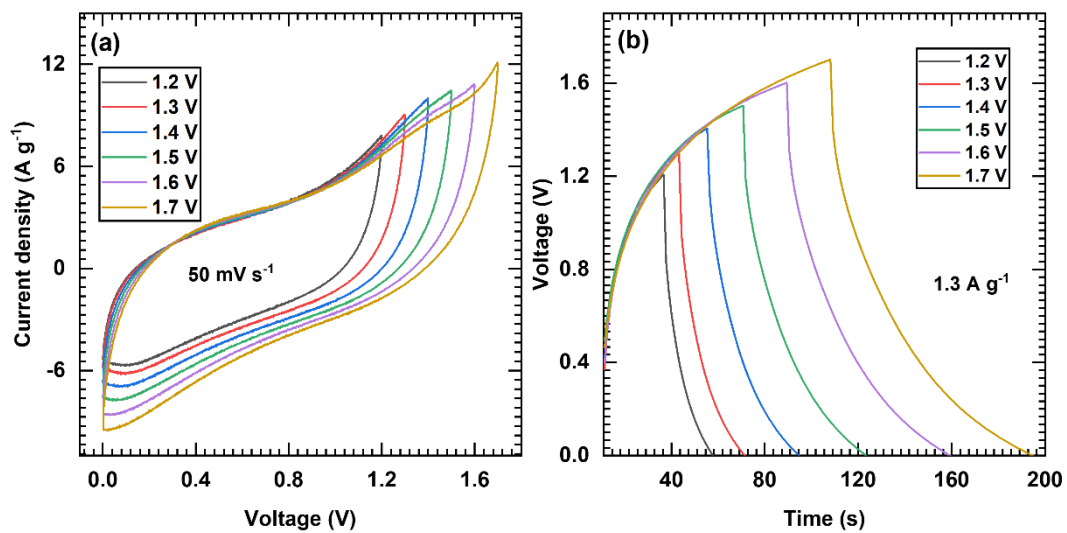**Fig. S14**

Fig. S15

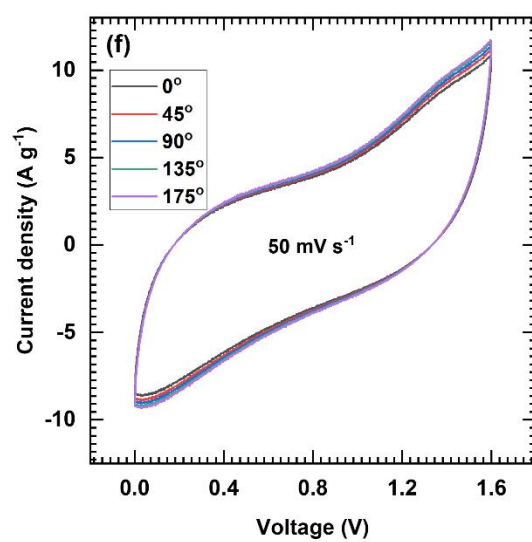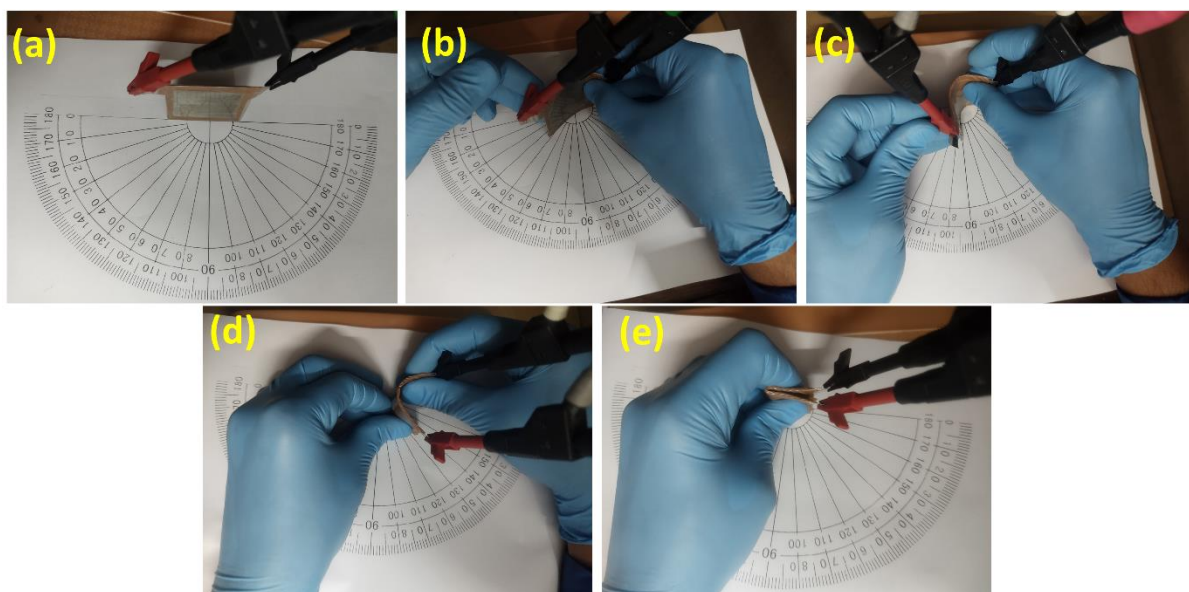**Fig. S16**

Fig. S17

Fig. S18

Sr. No.	Material	Method	Morphology	Electrolyte	Specific capacitance (F g^{-1}) at Current density	Stability cycles (capacitive retention %)	Current collector (Binder)	Ref.
1.	$Co_3V_2O_8$	Ion exchange process	Nanosheets	3 M KOH	878.9 at 1 A g^{-1}	5000 (95%)	Nickel foam (Binder-free)	[21]
2.	$Co_3V_2O_8$	Hydrothermal	Hollow spheres	1 M KOH	2376 at 2 A g^{-1}	10000 (97.4%)	Nickel foam (PVDF)	[22]
3.	$Co_2V_2O_7$	Ionothermal	Hexagonal nanoplates	2 M KOH	304.8 at 1 A g^{-1}	100 (103%)	nickel foam (PVDF)	[23]
4.	$Co_2V_2O_7 \cdot 3.3H_2O$	Co-precipitation	Microflowers	2 M KOH	351 at 1 A g^{-1}	30000 (103%)	Nickel foam (Polytetrafluorene)	[24]
5.	$Co_3V_2O_8$	Solvothermal	Rose-like	2 M KOH	353.6 at 1 A g^{-1}	7000 (89.6%)	Nickel foam (PVDF)	[25]
6.	$CoV_2O_6 \cdot 2H_2O$	Microwave irradiation	Nanosheets	6 M KOH	363 at 0.5 A g^{-1}	80000 (99.8%)	Nickel foam (PVDF)	[26]
7.	$Co_2V_2O_7$	Hydrothermal	Nanoparticles	-	285.6 at 0.5 mA g^{-1}	4000 (83.6%)	Nickel foam (PVDF)	[27]
8.	$Co_2V_2O_7$	Hydrothermal	Hexagonal sheets	4 M KOH	809 at 1 A g^{-1}	100000 (272%)	Nickel foam (Binder-free)	[28]
9.	$Co_3V_2O_8$	Hydrothermal	Nanosheets	6 M KOH	1320 at 1 A g^{-1}	10000 (89.1%)	Nickel foam (PVDF)	[39]
10.	$Co_3V_2O_8$	Chemical precipitation	Nanoparticles	2 M KOH	790 at 1 A g^{-1}	10000 (90.1%)	Nickel foil (PVDF)	[40]
11.	$Co_3V_2O_8$	Hydrothermal	Nanoplates	3 M KOH	739 at 0.5 A g^{-1}	2000 (95.3%)	Nickel foam (Polytetrafluoroethylene)	[R8]
12.	CoV_2O_6	Hydrothermal	Micron blocks	6 M KOH	114.1 at 1 A g^{-1}	1000 (81.9%)	Nickel foam (Polytetrafluoroethylene)	[R9]
13.	Co_2VO_4	Ion exchange process	Hollow Nanocubes	3 M KOH	427.6 at 1 A g^{-1}	10000 (89.3%)	Nickel foam (PVDF)	[R10]
14.	**$CoV_2O_6 \cdot 4H_2O$**	**Chemical bath deposition**	**Nanosheets**	**1 M KOH**	**845.3 at 1 A g^{-1}**	**10,000 (90.6%)**	**Stainless steel (Binder-free)**	**This work**

Table S1

Sample	Co%	V%	Co:V ratio
C-CV1	22.37	40.48	1:1.81
C-CV2	21.12	41.39	1:1.96
C-CV3	20.30	42.63	1:2.1
C-CV4	20.00	43.00	1:2.15
C-CV5	19.80	43.75	1:2.21

Table S2

Fitted Parameters	C-CV1	C-CV2	C-CV3	C-CV4	C-CV5
Rs (Ω)	0.93	0.63	0.96	0.92	1.31
Rct (Ω)	270	240	184	159	201.6
W-R (Ω)	0.0005	0.0015	0.0057	0.00047	0.00133
CPE-T (mF)	0.2	1.03	0.73	0.61	0.4
CPE-P (n)	0.8	0.85	0.7	0.73	0.7

Table S3

Fitted Parameters	AHSD (Before stability)	AHSD (After stability)	SH-FSD (Before stability)	SH-FSD (After stability)
Rs (Ω)	0.9	0.84	0.21	0.66
Rct (Ω)	138	294	130.5	194
W-R (Ω)	32.63	36.03	416.8	478
CPE-T (mF)	0.62	0.35	0.54	0.15
CPE-P (n)	0.83	0.85	0.73	0.57

Table S4

Sr. No.	Material	Method	Morphology	Electrolyte	Specific capacitance (F g^{-1}) at Current density	Specific Energy (Wh kg^{-1})	Specific Power (W kg^{-1})	Stability (%)	Ref.
1.	$Co_3V_2O_8$//AC	Precipitation	Nanosheet	3 M KOH	63 at 1 A g^{-1}	55.5	800	10000 (82.1%)	[21]
2.	$Co_3V_2O_8$//AC	Hydrothermal	Hollow spheres	6 M KOH	165.3 at 1 A g^{-1}	59.2	250	10000 (97.3%)	[22]
3.	$Co_2V_2O_7 \cdot 3.3H_2O$//rGO	Co-precipitation	Microflower	2 M KOH	60.7 at 1 A g^{-1}	19	375.8	10000 (96.4%	[24]
4.	$CoV_2O_6.2H_2O$//AC	One-step microwave	Doped block	6 M KOH	53 at 0.5 A g^{-1}	19	400	35000 (78.6%)	[26]
5.	$Co_2V_2O_7$//rGO	Hydrothermal	Nanosheet	4 M KOH	113 at 1 A g^{-1}	35.2	1001	10000 (71.4%)	[28]
6.	$Co_3V_2O_8$-$Ni_3V_2O_8$ TLs@PCNFs//PCNFs	Hydrothermal	Nanoneedles	3 M KOH	191 at 5 A g^{-1}	59.7	1970	3000 (88.5%)	[42]
7.	$Co_3V_2O_8$/CNT//AC	Hydrothermal	Nanospheres	1 M H_2SO_4	120.1 at 1 A g^{-1}	37.5	660	3000 (97.1%)	[51]
8.	$Co_3V_2O_8$/CN_x//AC	Solvothermal	Particles over sheets	2 M KOH	130.4 at 0.5 A g^{-1}	41	385.1	10000 (63.3%)	[52]
9.	Co_3O_4/CoV_xO_y//AC	Hydrothermal	Nanosheets-Nanowires	3 M KOH	73.3 at 0.5 A g^{-1}	26.1	400	5000 (77.4%)	[53]
10.	Co_3O_4/$Co_3(VO_4)_2$//AC	Hydrothermal	Nanorods	2 M KOH	105 at 0.5 A g^{-1}	38	275	5000 (94.7%)	[54]
11.	**$CoV_2O_6.4H_2O$//rGO**	**Chemical bath deposition**	**Nanosheets**	**1 M KOH**	**115 at 0.3 A g^{-1} (For AHSD)**	**40**	**1800**	**10,000 (86.3%)**	**This work**
					105.2 at 1.1 A g^{-1} (For SH-FSD)	**37.4**	**869**	**10,000 (83.3%)**	

Table S5

References:

[R1] M. Sethi, U. Shenoy and D. Bhat, *Nanoscale Adv.*, 2020, **2**, 4229-4241.

[R2] A. Bello, F. Barzegar, D. Momodu, J. Dangbegnon, F. Taghizadeh, M. Fabiane and N. Manyala, *J. Power Sources*, 2015, **273**, 305-311.

[R3] S. Marje, V. Patil, V. Parale, H. Park, P. Shinde, J. Gunjakar, C. Lokhande and U. Patil, *J. Chem. Eng.*, 2022, **429**, 132184.

[R4] D. Marcano, D. Kosynkin, J. Berlin, A. Sinitskii, Z. Sun, A. Slesarev, L. Alemany, W. Lu and J. Tour, *ACS Nano*, 2010, **4**, 4806.

[R5] S. Marje, P. Katkar, S. Kale, A. Lokhande, C. Lokhande and U. Patil, *J. Alloys Compd.*, 2019, **779**, 49-58.

[R6] H. Qiu, X. Sun, S. An, D. Lan, J. Cui, Y. Zhang and W. He, *Dalton Trans.*, 2020, **49**, 6391-6397.

[R7] Z. Le, F. Liu, P. Nie, X. Li, X. Liu, Z. Bian, G. Chen, H. Wu and Y. Lu, *ACS Nano*, 2017, **11**, 2952-2960.

[R8] Y. Zhang, Y. Liu, J. Chen, Q. Guo, T. Wang and H. Pang, *Sci. Rep.*, 2014, **4**, 5687.

[R9] Y. Teng, Y. Li, D. Yu, Y. Meng, Y. Wu, X. Zhao and X, Liu, *ChemistrySelect*, 2019, **4**, 956-962.

[R10] C. Li, D. Ma and Q. Zhu, *Nanomaterials*, 2022, **12**, 848.